33RD CONGRESS
OF THE INTERNATIONAL COUNCIL
OF THE AERONAUTICAL SCIENCES
STOCKHOLM, SWEDEN, 4–9 SEPTEMBER, 2022

ICAS 2022 SWEDEN

A NUMERICAL METHOD FOR STUDY ON THE AERO-ELASTICITY OF AIR-TO-AIR MISSILES IN OVER-THE-SHOULDER LAUNCH

Kuan Lu[1], Wen-Ping Song[1], Kun Ye[1], Chang-Hao Gao[1] & Shao-Qiang Han[2, 1]

[1]National Key Laboratory of Science and Technology on Aerodynamic Design and Research, School of Aeronautics, Northwestern Polytechnical University, Xi'an 710071, P. R. China
[2]College of Computer Science, Sichuan University, Chengdu 610065, P. R. China

Abstract

In order to analyze the aero-elasticity effect of air-to-air missiles during an unpowered over-the-shoulder launch (OTS launch), a computational fluid dynamics/computational structure dynamics/rigid body dynamics(CFD/CSD/RBD) coupling numerical method is developed, using a loose coupling strategy. The computational fluid dynamics (CFD) solver is based on structured overset grid, the computational structure dynamics (CSD) solver is based on a modal approach. The validation of the present method has been conducted by comparing with experimental data. CFD/CSD/RBD coupled simulation of the OTS launch is successfully performed on a simple missile model. The test case is that the missile drops at altitude of 12km with freestream Mach number of 0.8 with 25-degree tail deflection, and falls from static status bearing aero-dynamic load and gravity. The result shows that the aero-elasticity makes the missile vibrate continuously in the falling process and synchronously causes the vibration of the aerodynamic load in the early falling stage. However, Aero-elasticity does not have significant effect on the trajectory and attitude of the missile in this paper.

Keywords: over the shoulder launch, CFD/CSD/RBD coupling, aero-elasticity, unsteady flow

1. General Introduction

OTS launch is a launching technology for air-to-air missiles to hit the target behind the launching fighters. With OTS launch, fighters are enabled to aim targets from all directions. Utilizing the instability of missile during high angles of attack to carry out unpowered overturn is a new way of OTS launch. In this way, missiles are enabled to flip by 180 degrees more swiftly than conventional forward firing OTS launch[1].

However, this process is difficult to carry out numerical simulation. The moving missile continuously increases the angles of attack in the process of movement, and experiences from small angles of attack to large angles of attack, and finally points to the reverse tail forward. With aerodynamic force and flow characteristics changing rapidly, it requires valid computational fluid dynamics/rigid body dynamics (CFD/RBD) method to simulate the process. Yet, CFD/RBD method presumes the missile as rigid body and does not take aero-elasticity effect into consideration.

Slenderness ratio of air-to-air missiles has become rather large due to progress in materials science and limited space on their carriers. Thus, flexibility of air-to-air missiles has increased and it might not be appropriate to simply assume missile as a rigid body. Aero-elasticity effect has to be considered in numerical simulation. Therefore, a CFD/CSD/RBD coupling method is developed to study aero-elasticity of air-to-air missile in OTS launch.

Numerical method coupling CFD/CSD/RBD has been widely used studying effect of elastic deformation on rigid body motion and aerodynamic characteristics. Izhak Mizrahi[2] observed wing elasticity effects on store separation with ejection force; Hua RuHao[3] observed the effect of aero-elasticity of a missile on its trajectory by solving six-degree freedom dynamic equations and static aero-elastic equations; Wallenius and Lindberg[4] studied the launch of a rail wing-tip missile and investigated the effect of static wing elasticity on the missile separation process.

In this paper numerical method coupling CFD/CSD/RBD is developed to study aero-elasticity of air-to-air missile in OTS launch. CFD method is based on finite difference method with overset grid, CSD solver is based on modal approach, rigid body dynamics (RBD) is based on solving rigid body

dynamics equation.

2. Methodology

2.1 CFD Governing Equation and Numerical Methods

Differential form of fluid dynamics governing equation can be written as:

$$\frac{\partial Q}{\partial t}+\frac{\partial E}{\partial x}+\frac{\partial F}{\partial y}+\frac{\partial G}{\partial z}=\frac{\partial E_v}{\partial x}+\frac{\partial F_v}{\partial y}+\frac{\partial G_v}{\partial z} \tag{1}$$

In this paper, we apply finite difference method to governing equation. Coordinate transformation projecting physics space to computational space is adopted as follows:

$$\begin{aligned} x &= x(\xi,\eta,\zeta,\tau) \\ y &= y(\xi,\eta,\zeta,\tau) \\ z &= z(\xi,\eta,\zeta,\tau) \\ t &= \tau \end{aligned} \tag{2}$$

In order to perform CFD/CSD/RBD coupling simulation, near-body grids are always moving and morphing throughout the process, which means x is a function of ξ,η,ζ,τ. And the governing equation in computational space becomes:

$$\frac{\partial \tilde{Q}}{\partial t}+\frac{\partial \tilde{E}}{\partial \xi}+\frac{\partial \tilde{F}}{\partial \eta}+\frac{\partial \tilde{G}}{\partial \zeta}=\frac{\partial \tilde{E}_v}{\partial \xi}+\frac{\partial \tilde{F}_v}{\partial \eta}+\frac{\partial \tilde{G}_v}{\partial \zeta} \tag{3}$$

Where:

$$\tilde{Q}=J\begin{bmatrix}\rho\\ \rho u\\ \rho v\\ \rho w\\ E\end{bmatrix},\tilde{E}=J\begin{bmatrix}\rho U\\ \rho uU+\xi_x p\\ \rho vU+\xi_y p\\ \rho wU+\xi_z p\\ (E+p)U-\xi_t p\end{bmatrix},$$

$$\tilde{F}=J\begin{bmatrix}\rho V\\ \rho vV+\eta_x p\\ \rho vV+\eta_y p\\ \rho wV+\eta_z p\\ (E+p)V-\eta_t p\end{bmatrix},\tilde{G}=J\begin{bmatrix}\rho W\\ \rho uW+\zeta_x p\\ \rho vW+\zeta_y p\\ \rho wW+\zeta_z p\\ (E+p)W-\zeta_t p\end{bmatrix} \tag{4}$$

$$\begin{aligned} U &= \xi_t+u\xi_x+v\xi_y+w\xi_z, \\ V &= \eta_t+u\eta_x+v\eta_y+w\eta_z, \\ W &= \zeta_t+u\zeta_x+v\zeta_y+w\zeta_z \end{aligned} \tag{5}$$

$$\begin{aligned} \tau_{\xi 1} &= \tau_{11}\xi_x+\tau_{12}\xi_y+\tau_{13}\xi_z, \\ \tau_{\xi 2} &= \tau_{21}\xi_x+\tau_{22}\xi_y+\tau_{23}\xi_z, \\ \tau_{\xi 3} &= \tau_{31}\xi_x+\tau_{32}\xi_y+\tau_{33}\xi_z, \\ \tau_{\eta 1} &= \tau_{11}\eta_x+\tau_{12}\eta_y+\tau_{13}\eta_z, \\ \tau_{\eta 2} &= \tau_{21}\eta_x+\tau_{22}\eta_y+\tau_{23}\eta_z, \\ \tau_{\eta 3} &= \tau_{31}\eta_x+\tau_{32}\eta_y+\tau_{33}\eta_z, \\ \tau_{\zeta 1} &= \tau_{11}\zeta_x+\tau_{12}\zeta_y+\tau_{13}\zeta_z, \\ \tau_{\zeta 2} &= \tau_{21}\zeta_x+\tau_{22}\zeta_y+\tau_{23}\zeta_z, \\ \tau_{\zeta 3} &= \tau_{31}\zeta_x+\tau_{32}\zeta_y+\tau_{33}\zeta_z \end{aligned} \tag{6}$$

$$\varphi_1 = u\tau_{11} + v\tau_{12} + w\tau_{13} + k\frac{\partial T}{\partial x},$$
$$\varphi_2 = u\tau_{21} + v\tau_{22} + w\tau_{23} + k\frac{\partial T}{\partial y}, \quad (7)$$
$$\varphi_3 = u\tau_{31} + v\tau_{32} + w\tau_{33} + k\frac{\partial T}{\partial z}$$

$$\varphi_\xi = \varphi_1\xi_x + \varphi_2\xi_y + \varphi_3\xi_z,$$
$$\varphi_\eta = \varphi_1\eta_x + \varphi_2\eta_y + \varphi_3\eta_z, \quad (8)$$
$$\varphi_\zeta = \varphi_1\zeta_x + \varphi_2\zeta_y + \varphi_3\zeta_z$$

Where, ρ, u, v, w, T, E are density, velocity in x direction, velocity in y direction, velocity in z direction, temperature, total energy respectively; U, V and W are contravariant velocity in ξ, η, ζ direction respectively; $\tau_{\xi 1}, \tau_{\xi 2}, \tau_{\xi 3}$ are shear stress in ξ direction; $\tau_{\eta 1}, \tau_{\eta 2}, \tau_{\eta 3}$ are shear stress in η direction; $\tau_{\zeta 1}, \tau_{\zeta 2}, \tau_{\zeta 3}$ are shear stress in ζ direction; $\varphi_\xi, \varphi_\eta, \varphi_\zeta$ are flux cause by due to viscous stress and thermal conduction.

CFD solution is based on RANS method. SST model is chosen as turbulence model. Roe upwind scheme is chosen as space discrete scheme and LU-SGS scheme is chosen as time discrete scheme.

2.2 Overset grid topology

In order to couple 6 DOF (6 degrees of freedom) movement and structural dynamic movement, high quality overset grid is adopted in the simulation. In this paper, a strategy of combining near-body grid and background grid is adopted. Hyperbolic grid is adopted as body-fitted near body grid in order to achieve better orthogonality. Cartesian grid is adopted as background grid. For Cartesian grid is static and does not move over time, grid morphing and 6 DOF movement are only applied on near-body grid.

2.2.1 Hole cutting method

Currently many methods have been adopted as hole cutting methods. In this paper, object x-rays method[5] has been applied as hole cutting method. Object x-rays method is a hybrid method of hole mapping method and ray casting method which requires much less memory than hole mapping method and has higher efficiency than ray casting method. The calculation of object x-rays method does not increase with the increase of x-rays. Thus, we can have high resolution hole for complex object and does not need to pay more calculation in hole cutting process. Advantages above make object x-rays method an ideal way for hole cutting of overset grid.

2.3 CFD/CSD coupling method

2.3.1 Structural Dynamic Equation

In this paper, structural dynamic function is solved in modal coordinates[6]. Structural dynamic equation in modal coordinates is defined as:

$$[M]\ddot{\xi} + [G]\dot{\xi} + [K]\xi = F \quad (9)$$

Where, $[M]$ is general mass matrix, $[G]$ is general damping matrix, $[K]$ is general stiffness matrix, F is general force vector, ξ is general coordinate vector, $\dot{\xi}$ is the first order derivatives of general coordinates respect of time and $\ddot{\xi}$ is the second order derivatives of general coordinates respect of time .

2.3.2 Runge-Kutta time stepping method

In order to solve structural dynamic modal equation, 4-step Runge-Kutta time marching method is adopted. Firstly, we covert equation above as follows:

$$\dot{\mathrm{E}} = \mathrm{A}\cdot\mathrm{E} + \mathrm{B}\cdot\mathrm{F}(\mathrm{E}, \mathrm{t}) \quad (10)$$

Where:

$$A=\begin{bmatrix} O & I \\ -M^{-1}K & -M^{-1}G \end{bmatrix}, \mathrm{B}=\begin{bmatrix} O \\ M \end{bmatrix}$$

So that the second order differential equations are converted to first order differential equations, and Runge-Kutta time marching method can be applied as follows:

$$\begin{aligned} E_{n+1} &= E_n + (k_1 + 2k_2 + 2k_3 + k_4)/6 \\ k_1 &= \Delta t \cdot [A \cdot E_n + B \cdot F(t)] \\ k_2 &= \Delta t \cdot [A \cdot (E_n + k_1/2) + B \cdot F(t + \Delta t/2)] \\ k_3 &= \Delta t \cdot [A \cdot (E_n + k_2/2) + B \cdot F(t + \Delta t/2)] \\ k_4 &= \Delta t \cdot [A \cdot (E_n + k_3) + B \cdot F(t + \Delta t)] \end{aligned} \tag{11}$$

In equation(11), $F(t+\Delta t/2)$, $F(t+\Delta t)$ are general force vectors of physical time $t+\Delta t/2, t+\Delta t$. However general force vector is obtained by CFD solver and it would cost too much calculation to obtain general force vector in advance. So the program obtains $F(t+\Delta t/2)$, $F(t+\Delta t)$ by building a quadratic function interpolation model according to $F(t-2\Delta t), F(t-\Delta t), F(t)$.

2.3.3 RBF grid morphing method

Currently, various grid morphing methods[7][8] are developed. Among which, grid morphing method based on radius based function(RBF) is widely used, for which is more robust and has less effect on grid quality. Deformation of an arbitrary CFD grid point can be expressed as:

$$d(x) = \sum_{i=1}^{n} w_i \varphi(\|x - x_i\|) \tag{12}$$

The deformation of an arbitrary CFD grid is calculated as the sum of a function of Euclidean distance to every control points with different weights. In equation (12), $\|x - x_i\|$ is distance from CFD grid point to the i^{th} control point in RBF model, w_i denotes for weight of the i^{th} control point in RBF model.

2.4 CFD/RBD coupling method

Rigid body translation can be solved by Newton second law as below:

$$F = m\frac{d^2x}{dt^2} \tag{13}$$

While rigid body rotation is formulated in the body local coordinate system (with the origin at the center of mass of the body) as below:

$$[I]\frac{d\omega}{dt} + \omega \times [I]\omega = M \tag{14}$$

Where $[I]$ denotes for matrix of moment of inertia, M denotes for total moment inserted on rigid body, ω denotes for angular velocity of body local coordinate system.

2.5 CFD/CSD/RBD coupling routine

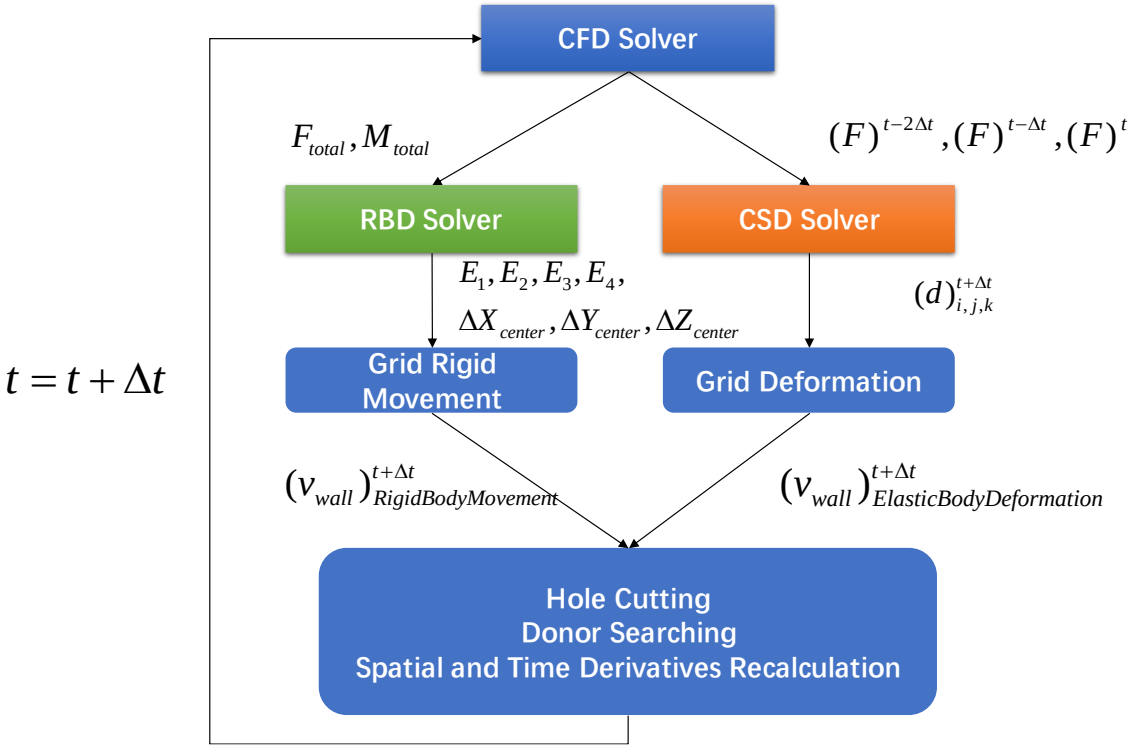

Figure 1 - CFD/CSD/RBD Coupling Routine

The CFD/CSD/RBD coupling routine is demonstrated above. Loose coupling is adopted throughout simulation. As it is shown in Figure 1, after CFD sub-iterations for solution of time step t, CFD solver pass aerodynamic force and moment to CSD solver and RBD solver respectively. For loose coupling is applied, CSD solver and RBD solver work independently.

As for RBD solver, coupling program get total force and moment from CFD solver and solve for rigid body motion and speed. On the other hand, CSD solver gets general force from CFD solver and solves for grid deformation and grid speed of grid deformation. Since grid coordinates and moving speed have been changed, time and spatial metrics for near-body grids will be recalculated and donors will be searched for overset boundary. After all these procedures, the program moves on to next CFD time step iterations.

3. Numerical Method Validation

3.1 CFD/CSD coupling method validation

HIRENASD (high Reynolds number aero-structural dynamics) [9][10] wing-body configuration model has been widely used as a standard model to validate method of CFD/CSD coupling. At Mach number of 0.8, Reynold number of 7.0E6, angle of attack of 1.5 degrees, calculation result is demonstrated below. In Figure 2 and Figure 3, CFD grid and displacement contour are demonstrated respectively. In Figure 4, pressure coefficient of two sections of the wing are compared with experiment data. Pressure coefficient calculated according to present method agrees to experiment data, which shows that CFD/CSD coupling method in this paper is valid.

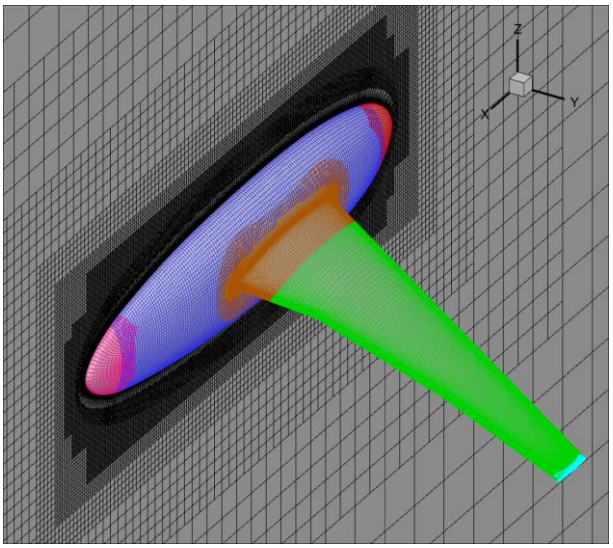

Figure 2 - CFD grid of HIRENASD model

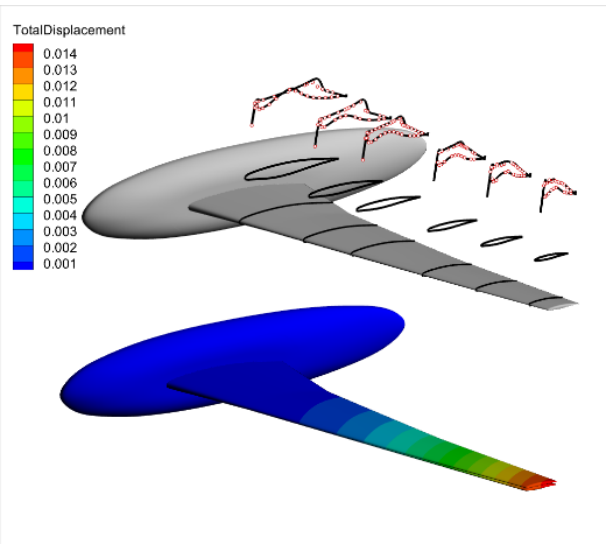

Figure 3 - Deformation contour of HIRENASD model

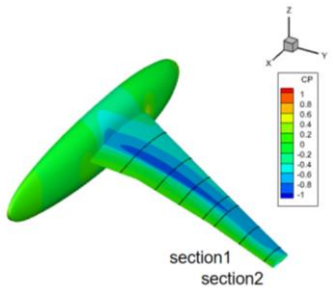

(a) Pressure coefficient contour

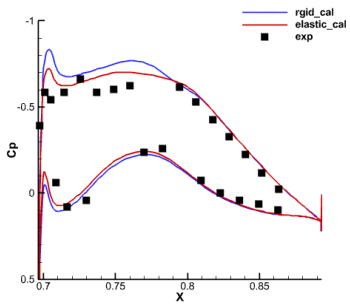

(b) Cp distribution of section1

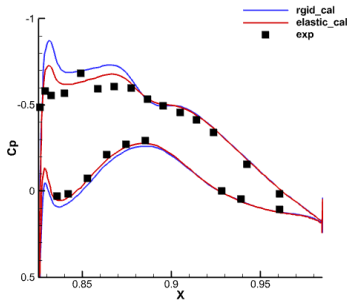

(c) Cp distribution of section2

Figure 4 - Pressure coefficient compared with experiment data

3.2 CFD/RBD coupling method validation

Wing/Pylon/Finned Store (WPFS) model[11] has been widely used as a standard model to validate method of CFD/RBD coupling. It has sufficient experiment data including rigid body transition data and attitude variation in Euler angles. Figure 5 shows the overset grid of WPFS model, Figure 6 shows the results of WPFS model compared to experiment data. We can see that the results from calculation have good agreement with the experiment data and the accuracy is satisfying. Therefore, the CFD/RBD coupling method in this paper is valid.

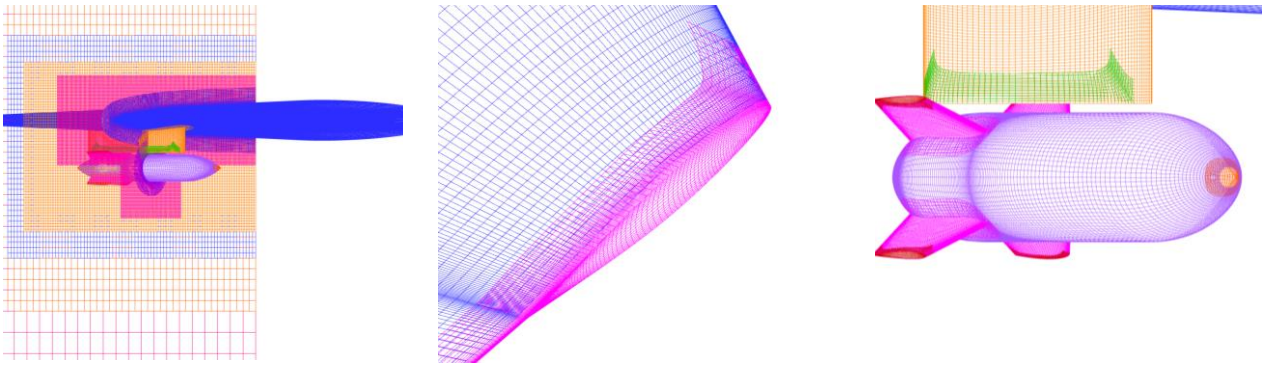

Figure 5 – Overset grid of WPFS

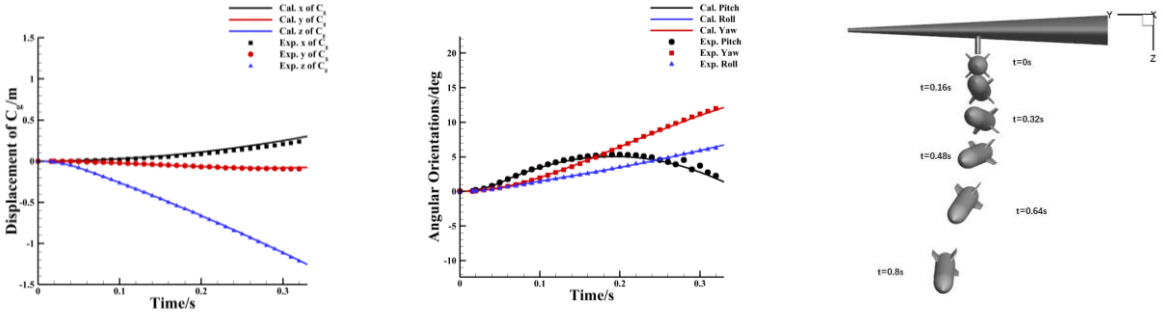

(a) Rigid body transition (b) Rigid body movement (c) Missile trajectory

Figure 6 - Result of WPFS model compared to experiment data

4. OTS Launch Numerical Simulation

Dynamic aero-elasticity characteristics of a missile have been analyzed by performing CFD/CSD/RBD coupling simulation. The geometry of the missile is shown below. Missile model is a combination of a body and x configuration tails. Mach number of 0.8 at attitude of 12km is chosen as free stream condition. To achieve fast overturn without active control, the deflection of missile tails is set to 25 degrees during the simulation. Because this tail-configured missile is statically stable at small angles of attack, it would not accomplish fast overturn without any control measures. Although the missile becomes instable at high angles of attack, it still has to overcome the statically stable period when the change of aero-dynamic moment damps the change of missile's attitude. In this paper, in order to obtain pitching motion from aerodynamic moment only, the angle of deflection of tails are set to 25 degrees, demonstrated in Figure 7.

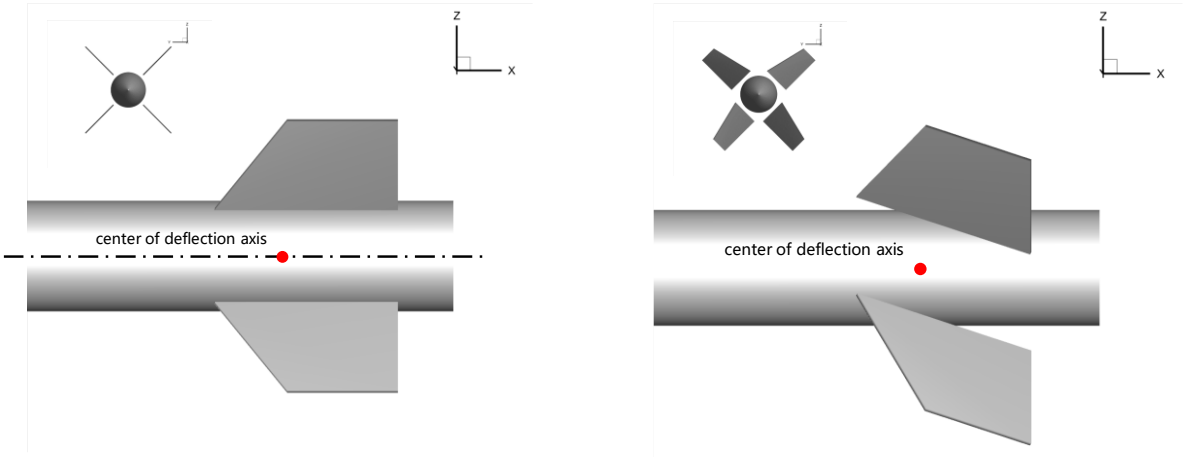

(a) Tails with no deflection (b) Tails with 25-degree deflection

Figure 7 – Deflection of tails

4.1 Overset Gird generation

In order to maintain robust and accurate CFD solution, hyperbolic grid is adopted as near-body grid, and Cartesian grid is adopted as background grid. Surface grid of the missile is shown below. As it is shown in Figure 8 and Figure 9, there are 17 near-body blocks in the grid system (5 blocks on missile body and 3 blocks on each tail). The grid system has grid points of 7.5 million.

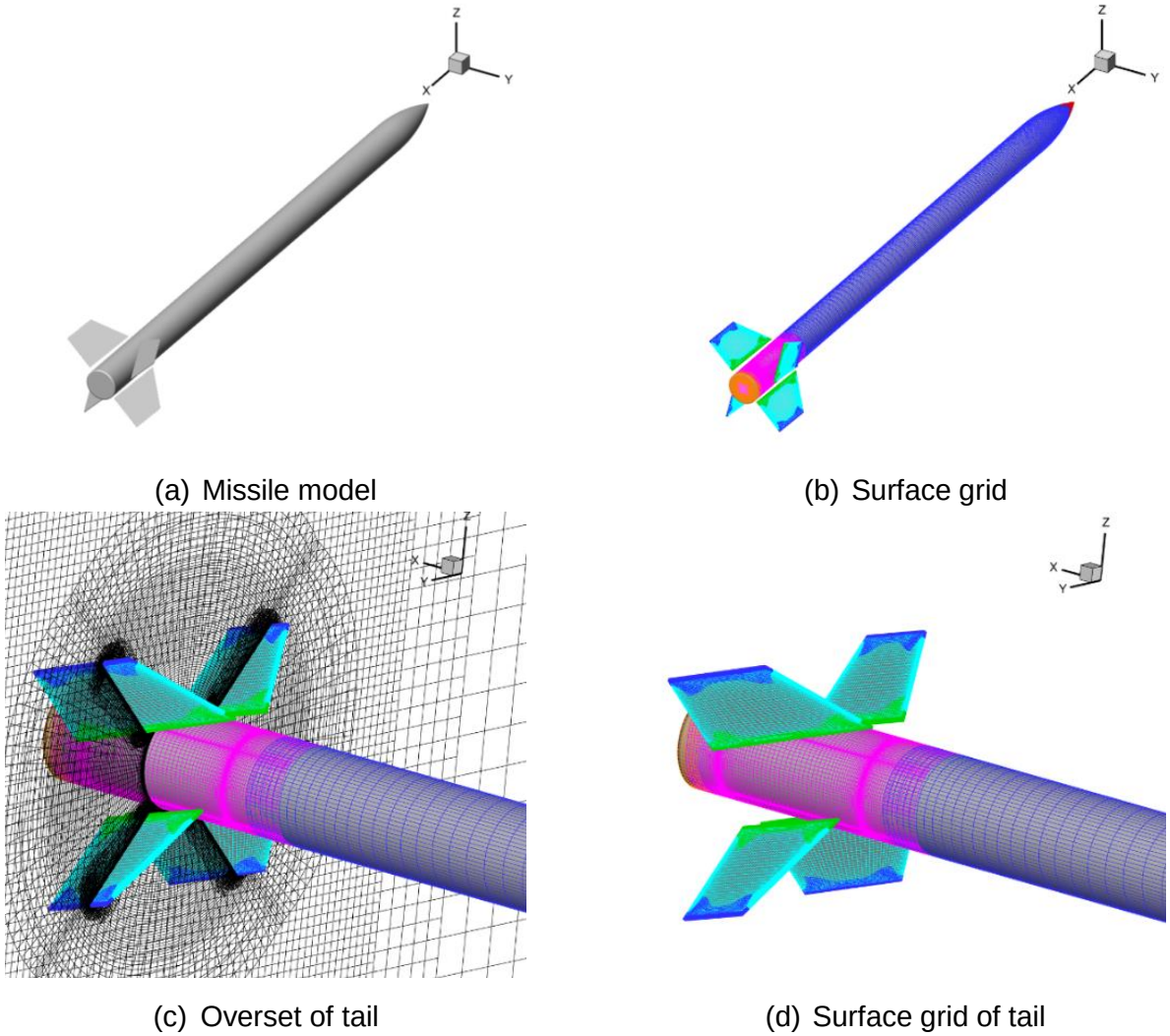

(a) Missile model (b) Surface grid

(c) Overset of tail (d) Surface grid of tail

Figure 8 - CFD grid of the missile

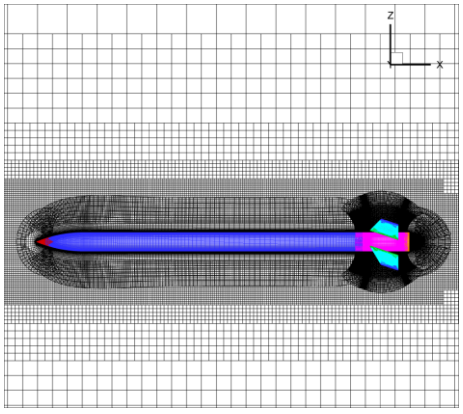

Figure 9 - CFD grid topology demonstration

4.2 Modal Analysis

Modal shapes are obtained by finite element method. A simple finite element model of the missile body is constructed by a beam model with mass distribution and bending stiffness presumed according to structure and material of a conventional air-to-air missile. The first three orders of bending modes are shown in Figure 10. For the missile body is regarded as an axis symmetry structure, there are three modes in both lateral direction and normal direction.

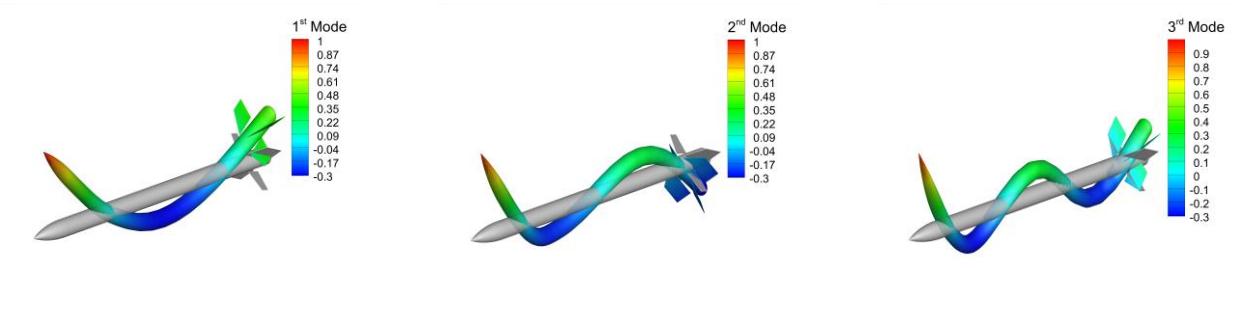

(a) 1st modal (b) 2nd modal (c) 3rd modal

Figure 10 - Modal shape of the missile in lateral direction

4.3 Results of OTS launch numerical simulation

The trajectory of the rigid and elastic missile are shown in Figure 11 -Figure 13 by taking snapshots of missile every 0.1 second. In Figure 11 and Figure 12, the trajectory of elastic missile and rigid missile are similar, therefore aero-elasticity does not have significant effect on missile trajectory. Both of these two missiles start pitching at 0 s due to moment caused by deflection of tails. Due to being lack of power, the missiles keep moving backwards relative to the freestream coordinate system. In this process, both of the missiles mainly move in the XZ plane and have little translation in Y direction and little rotation in rolling and yawing direction. In Figure 13 trajectories are compared with each other by coloring elastic missile red and rigid missile black. Elastic missile has smaller pitching angle at the end of simulation.

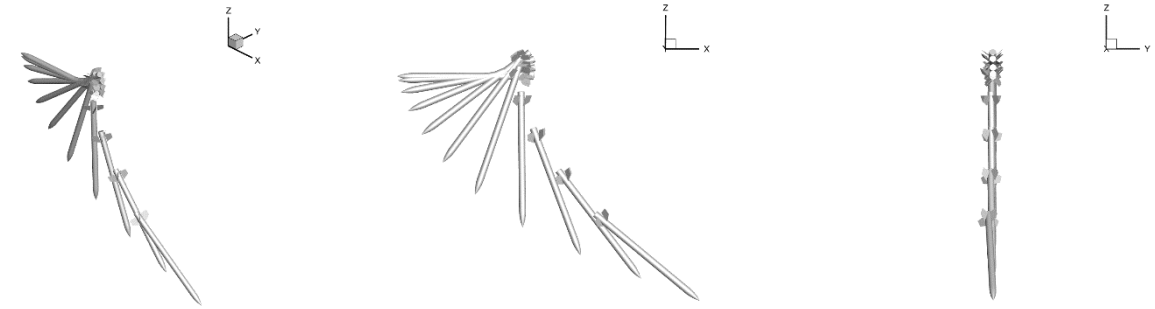

Figure 11 - Rigid missile trajectory

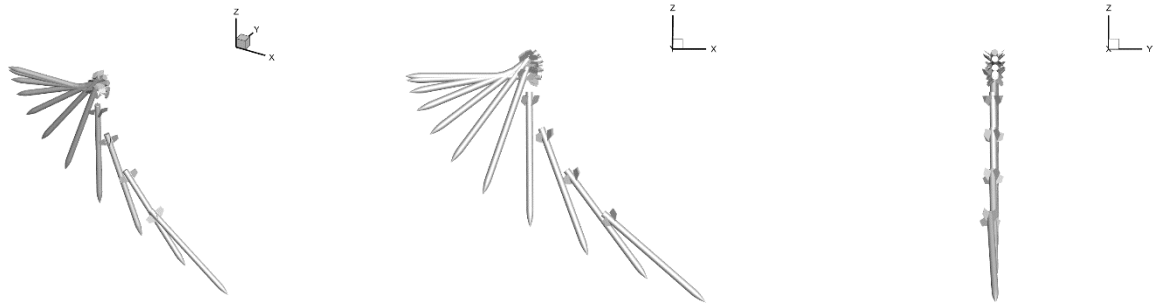

Figure 12 - Elastic missile trajectory

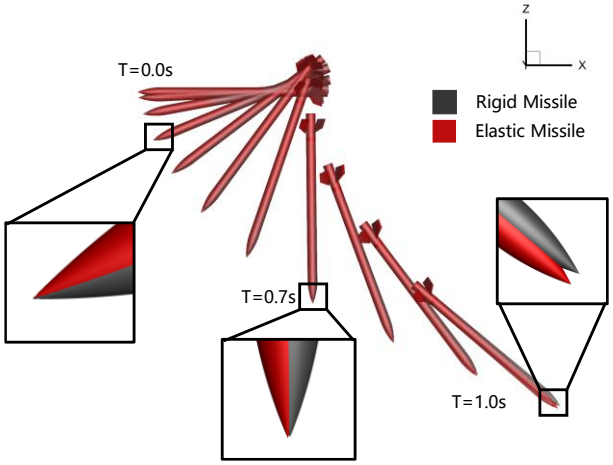

Figure 13 – Rigid and elastic missile trajectory

Figure 14 shows body translation of both rigid and elastic missile and Figure 15 shows body translation change due to aero-elasticity. In Figure 14 body translation of rigid and elastic missile coincide with each other and body translation change is on the order of centimeters. In Figure 15, body translation in x and y direction are rather small and body translation change in z direction is getting bigger due to aero-elasticity. For body translation in Z direction is negative, aero-elasticity amplifies the body translation in this OTS launch. Thus, compared to trajectories which is on the order of meters, aero-elasticity has rather small effect on body translation.

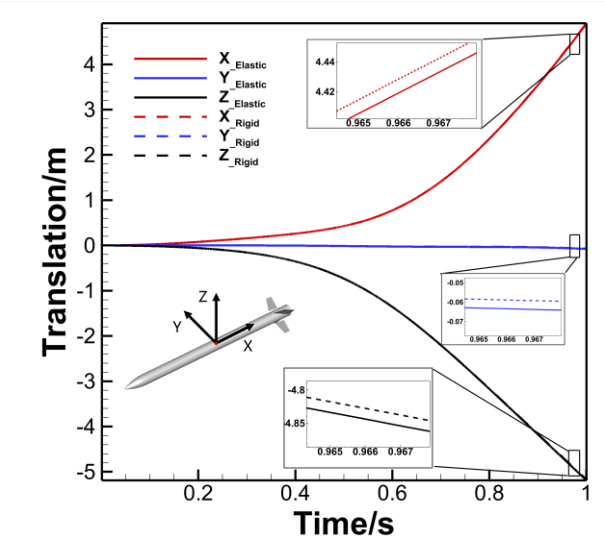

Figure 14 – Missile body translation

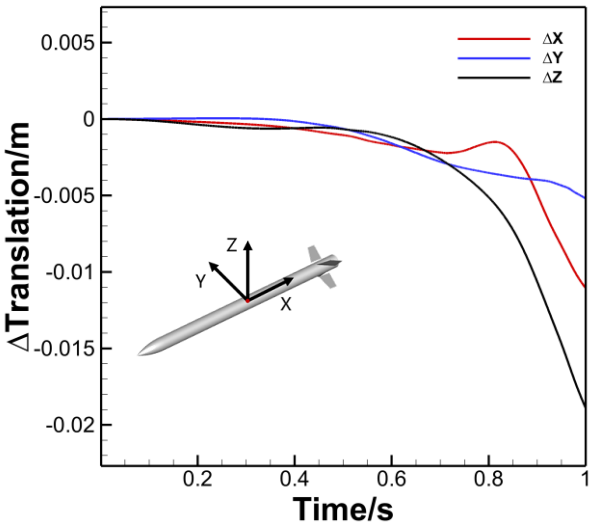

Figure 15 – Missile body translation change due to aero-elasticity

Figure 16 to Figure 18 show displacement of the first three bending modes in normal direction of the elastic missile in OTS launch. The missile drops with initial general displacement of 0. The aerodynamic force caused by deflection of tail and aerodynamic load on missile body leads to a non-zero general forces, which excite the vibration of missile. Due to different modal shapes and different general frequencies, the displacement of first three modes of missile body have different displacement. In the whole process, the displacement of the first mode dominates the deformation, as shown in Figure 16. The balance position of vibration of the first mode varies slightly with time. In Figure 17, the second general coordinate keeps oscillating at smaller amplitude but higher frequency. In Figure 18, the displacement of third mode converges with time.

Figure 19 shows general displacement of first three modes in lateral direction. The missile drops with initial general displacement of 0 in lateral direction too. Before 0.3s, the general forces in lateral direction are rather small because the aerodynamic load is almost symmetric in Y direction. Due to flow separation caused by 25 degree-deflection of tails, the aero-dynamic load is not strictly symmetric in Y plane at the initial state. Moreover, with the proceeding of pitching motion, the asymmetric effect

grow more and more significant and causes much bigger general force in lateral direction than the initial state when the missile just begins to drop. Nevertheless, the displacements in lateral direction are smaller than those in normal direction by one or even more orders of magnitude.

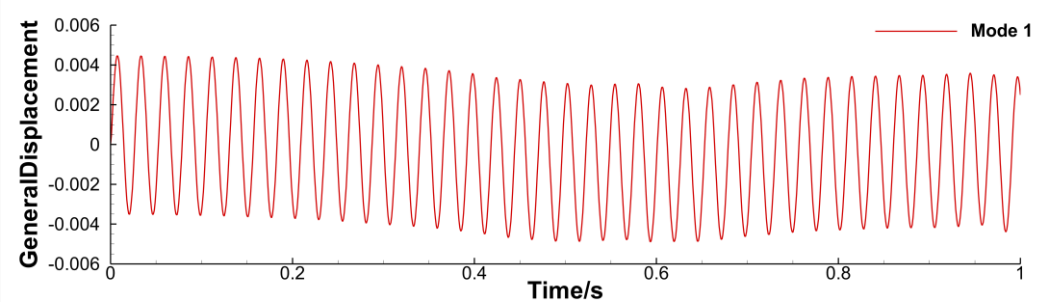

Figure 16 - General displacement of mode 1 in normal direction

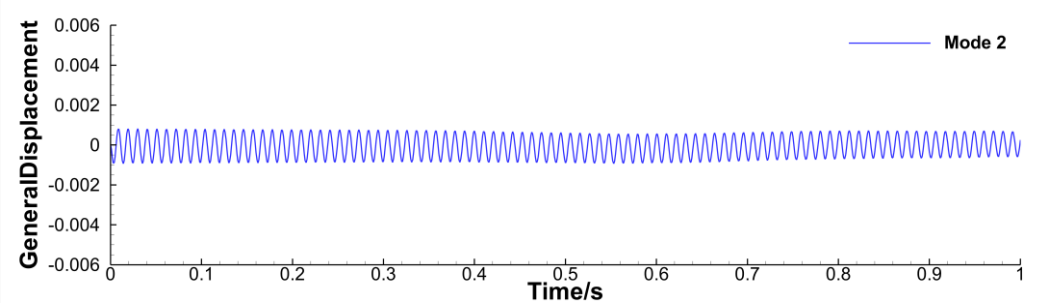

Figure 17 - General displacement of mode 2 in normal direction

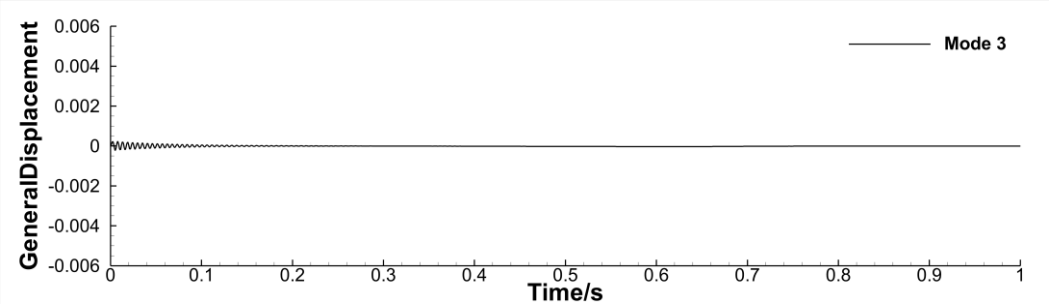

Figure 18 - General displacement of mode 3 in normal direction

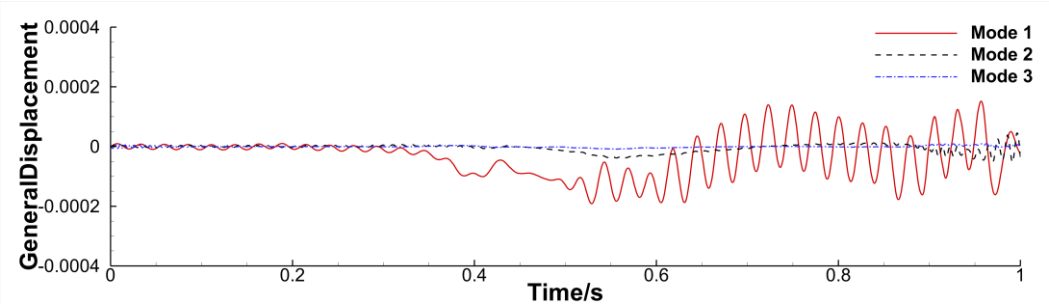

Figure 19 - General displacement of fist three modes in lateral direction

Figure 20 shows aero-elasticity effect on aero-dynamic force. Generally, aerodynamic forces of the elastic and the rigid missile coincide with each other in X and Z direction during the simulation. During 0s to 0.5s, the aerodynamic forces of the elastic missile quiver around the aerodynamic forces of the rigid missile. Aerodynamic forces in Y direction of the rigid missile and the elastic missile jump up and down rapidly from 0.8s to 1.0s.

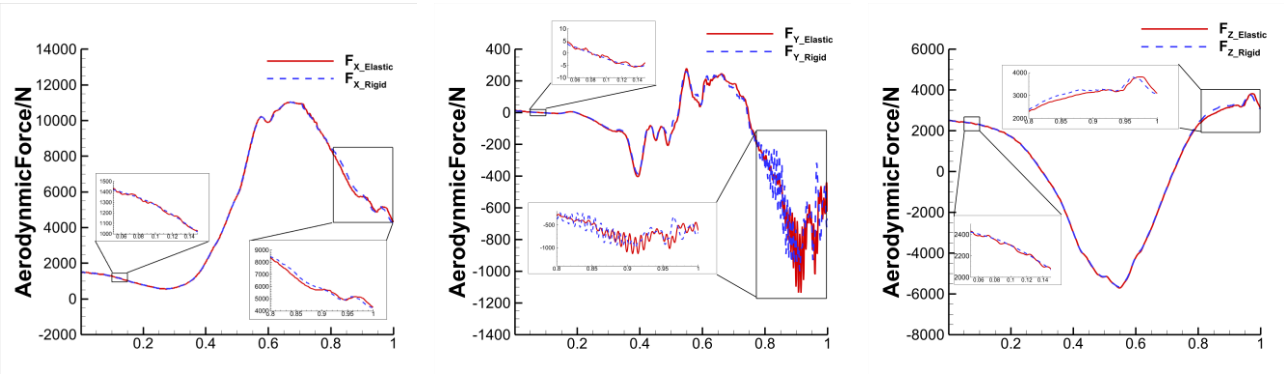

(a) F_X (b) F_Y (c) F_Z

Figure 20 – Aerodynamic Force

Figure 21 shows aero-elasticity effect on aero-dynamic moment. The moment reference point is taken at center of mass. In Figure 21 ,aerodynamic moment is rather small in direction of X and Z in the first 0.5 s. Due to asymmetry flow in high angles of attack, after 0.5 s, moments in direction of X and Z begin to increase. There is a period when moments in X and Z direction jump up and down rapidly with respect of time from 0.8s to 1s.

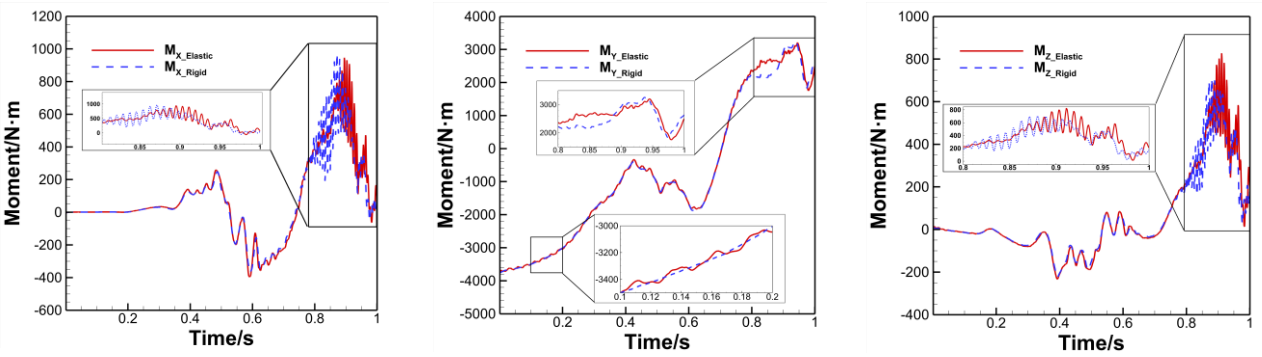

(a) M_X (b) M_Y (c) M_Z

Figure 21 – Aerodynamic Moment

From Figure 20 and Figure 21, we observe severe vibrations of aerodynamic force in Y direction and aerodynamic moment in X and Z direction from 0.8s to 1.0s for both missiles. Though the phenomenon does not have significant effects on missiles' trajectories, the mechanism is worth further discussion. In Figure 22, aerodynamic force in Y direction and aerodynamic moments in X and Z direction of the rigid missile from 0.8s to 1.0s are depicted. The frequency of vibration of these forces and moments are identical. Therefore, the vibration of these forces and moments are caused by the same kind of periodic unsteady flow in the flow field.

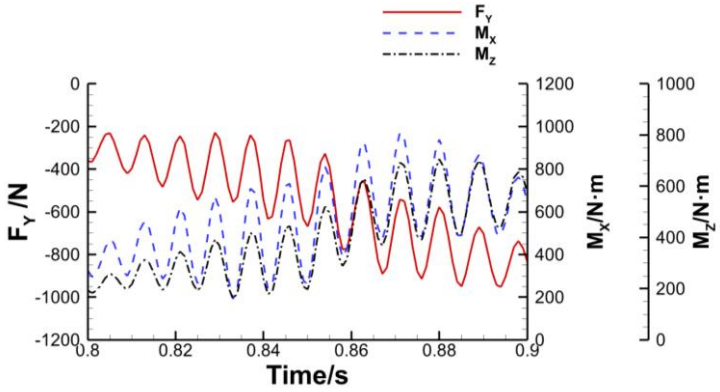

Figure 22 – Aerodynamic Force and Moment of the Rigid Missile from 0.8s to 1.0s

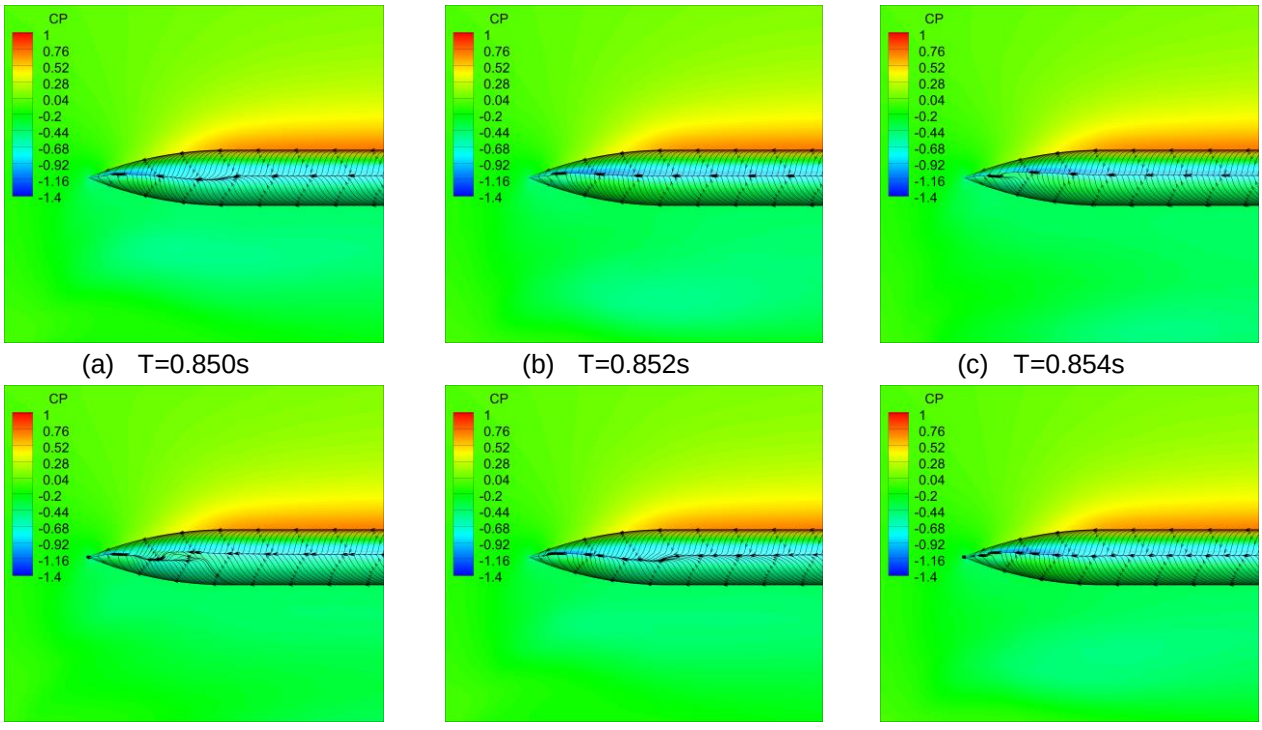

(a) T=0.850s (b) T=0.852s (c) T=0.854s

(d) T=0.856s (e) T=0.858s (f) T=0.860s

Figure 23 – Limiting Streamlines on Rigid Missile Head

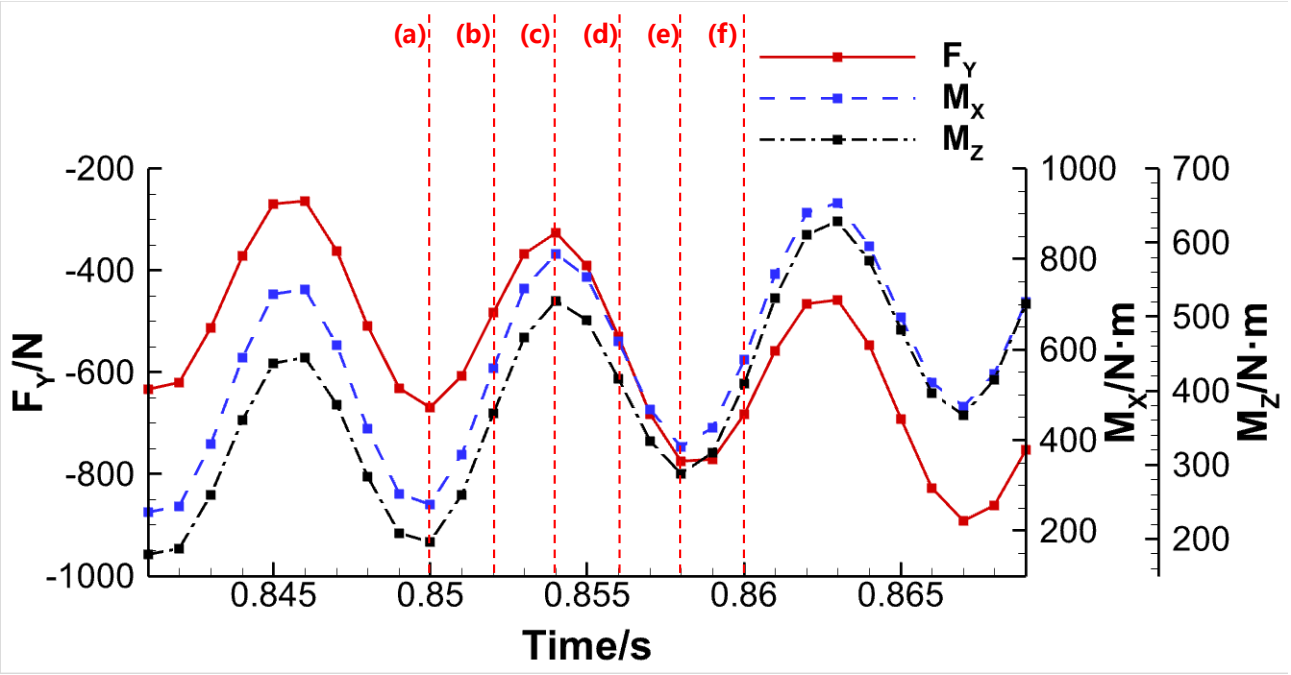

Figure 24 –Aerodynamic Force and Moment of the Rigid Missile from 0.84s to 0.87s

Figure 23 shows the limiting streamline on the missile head of rigid missile from 0.850s to 0.860s. The changing pattern of flow separation line and aero-dynamic loads are almost the same. The detailed variance is analyzed by 6 steps as follows.

(1)Figure 23 (a) shows limiting streamline on the missile head at 0.850s. Flow separation line is twisted on the missile head at t=0.850s and becomes less twisted with the increase of time. Since then the aerodynamic force reaches a trough of oscillation at t=0.850s, which can be seen in Figure 24.

(2)Figure 23 (b) shows limiting streamline on the missile head at 0.852s. In Figure 23 (b), flow separation line is calming down on the middle of missile head. Meanwhile a new wave appears at the head tip of the missile.

(3) Figure 23 (c) shows limiting streamline on the missile head at 0.854s. In Figure 23 (c), flow separation line is parallel to central axis of the missile body, which makes aerodynamic force reach a peak of oscillation in Figure 24. Yet the new wave from the missile head is not fully spread.

(4) Figure 23 (d) shows limiting streamline on the missile head at 0.856s. In Figure 23 (d), the new wave induces a second separation line near the missile's head tip. The missile head and flow separation line starts to be twisted again.

(5) Figure 23 (e) shows limiting streamline on the missile head at 0.858s. In Figure 23 (e), the new wave is fully spread and flow separation line is rather twisted and it is similar to Figure 23 (a),which makes aerodynamic force reach a trough of oscillation in Figure 24.

(6) After 0.002s, Figure 23 (f) shows that this pattern repeats again.

From this pattern, a conclusion is drawn that the oscillation of aerodynamic load is caused by unsteady flow separation induced from the missile head at a high angles of attack, which is demonstrated from the variance of flow separation line with time.

5. Conclusion

A coupled CFD/CSD/RBD simulation method is developed to carry out complex numerical simulation such as OTS launch. With this method, we successfully simulated the process of unpowered OTS launch and observed the effect of aero-elasticity on the tail configured missile. For the missile in this paper, conclusions are as follows:

- Aero-elastic deformation of the missile in this paper is not significant. During the OTS launch, the elastic deformation of the missile is dominated by the first and second bending mode and the missile keeps vibrating with small amplitude.
- Aero-elasticity of the missile in this paper has only slight effects on the trajectory and attitude.
- Although the deformation of the aero-elasticity is not significant, the vibration still leads to some changes in aerodynamic characteristics. In the initial period of OTS launch, aerodynamic force and moment of the elastic missile quiver around which of rigid missile with structural vibration of the elastic missile.

However, in this paper, some simplification has been made which worth further study:

- The missile geometry and structural finite element model are quite simple, which may not be adequate for realistic OTS launch simulation. More complex geometry and more reasonable finite element model will be introduced in the future work.
- The carrier of missile and ejection force from the carrier is not included in this simulation.
- Aero-elasticity of the missile in this paper does not have significant effect on the OTS launch. This might be due to the high stiffness of missile structure in present test case. With different structural characteristics, aero-elasticity may have different effects in OTS launch.

Future work will focus on adding more functions on the coupled CFD/CSD/RBD solver for simulation of more complex motions (with carrier and ejection force and more complex missile geometry) and studying the mechanism of aero-elastic effect on OTS launch.

6. Acknowledgment

This study was funded by the National Natural Science Foundation of China (NSFC) under the Grant No. 11902261, the Fundamental Research Funds for the Central Universities of China under the Grant No. D5000220178, the Foundation of National Key Laboratory of Science and Technology on Aerodynamic Design and Research (No. 614220121030224)

7. Contact Author Email Address

Wen-Ping Song: wpsong@nwpu.edu.cn

8. Copyright Statement

original material included in this paper. The authors also confirm that they have obtained permission, from the copyright holder of any third party material included in this paper, to publish it as part of their paper. The authors confirm that they give permission, or have obtained permission from the copyright holder of this paper, for the publication and distribution of this paper as part of the ICAS proceedings or as individual off-prints from the proceedings.

References

[1] Jin Y H，Wu H C，Yu Z K．Research on Tossing-Orientation Scheme of Over-the-Shoulder Launch and Control Technology．*Aero Weaponry*，Vol. 28, No. 3, pp. 59–64. 2021.

[2] Mizrahi I, and D. E. Raveh. Wing Elasticity Effects on Store Separation. *Journal of Aircraft*, Vol. 56, No 3 pp 1231-1249 2019.

[3] Hua R, Zhao C, Ye Z, Jiang Y. Effect of elastic deformation on the trajectory of aerial separation. *Aerospace Science and Technology*, Vol. 45, pp 128-139, 2015

[4] Wallenius H, and A Lindberg. MAJOR IMPROVEMENTS IN STORES SEPARATION ANALYSIS USING FLEXIBLE AIRCRAFT. *Congress of the International Council of the Aeronautical Sciences*, 2010. Sweden

[5] Meakin, R. Object X-rays for cutting holes in composite overset structured grids. *15th AIAA Computational Fluid Dynamics Conference*, 2001.

[6] Chen D, Yang G. STATIC AEROELASTIC ANALYSIS OF A FLYING-WING USING DIFFERENT MODELS. *Chinese Journal of Theoretical and Applied Mechanics*, Vol. 41, No 4, pp 469-479, 2009.

[7] Rendall T C S, Allen C B. Efficient mesh motion using radial basis functions with data reduction algorithms. *Journal of Computational Physics*, Vol. 228, No 17, pp 6231-6249, 2009

[8] Zhang Weiwei, Gao Chuanqiang, Ye Zhengyin. Research progress on mesh deformation method in computational aeroelasticity. *Acta Aeronautica et Astronautica Sinica*, Vol. 35, No 2, pp 303-319

[9] Ballmann, J. Experimental Analysis of high Reynolds Number structural Dynamics in ETW. *46th AIAA Aerospace Sciences Meeting and Exhibit*, 2008

[10] Mian, H. H. RBF interpolation with improved data reduction algorithm — A meshfree method for fluid-structure coupling and mesh deformation. *IEEE*, pp 234-242, 2014.

[11] Tang Z G, Li B, Zheng M. Store separation simulation using overset unstructured grid. *Acta Aerodynamica* Sinica, Vol. 27, No 5, pp 593-596, 2009.